Quantitative phase and refractive index analysis of optical fibers using differential interference contrast microscopy

Betty Kouskousis,[1,*] Daniel J. Kitcher,[1] Stephen Collins,[1] Ann Roberts,[2] and Greg W. Baxter[1,3]

[1]Optical Technology Research Laboratory, Centre for Telecommunications and Microelectronics, Victoria University, P.O. Box 14428, Melbourne, Victoria 8001, Australia

[2]School of Physics, University of Melbourne, Melbourne, Victoria 3010, Australia

[3]E-mail: gregory.baxter@vu.edu.au

*Corresponding author: betty.kouskousis@live.vu.edu.au

A systematic and straightforward image processing method to extract quantitative phase and refractive index data from weak phase objects is presented, obtained using differential interference contrast (DIC) microscopy. The method is demonstrated on DIC images of optical fibers where a directional integration routine is applied to the DIC images to extract phase and refractive index information using the data obtained across the whole DIC image. By applying the inverse Abel transform to the resultant phase images, an accurate refractive index profile is obtained. The method presented here is compared to the refracted near-field technique, typically used to obtain the refractive index profile of optical fibers, and shows excellent agreement. It is concluded that through careful image processing procedures, DIC microscopy can be successfully implemented to obtain quantitative phase and refractive index information of optical fibers.   © 2008 Optical Society of America

OCIS codes: 060.2270, 060.2300, 070.6110, 100.2960, 100.5070, 110.0180.

1. Introduction

The refractive index profile of an optical fiber is of fundamental significance since from it important characteristics can be determined, such as the mode field profile, cutoff wavelength, and dispersion. A number of methods have been developed to monitor the refractive index profile of an optical fiber. Currently the industry standard is the refractive near-field (RNF) method [1]. Although this is the most widely used technique, limitations include the inability to measure rapidly varying refractive index along the fiber axis, important for optical devices such as fiber Bragg gratings (FBGs). Additionally the RNF technique is destructive since the fiber must be cleaved. Other techniques used to determine the refractive index profile of optical fibers have been demonstrated [1–5]. Recently it has been established that differential interference contrast (DIC) microscopy can be used to acquire the refractive index profile of optical fibers with results comparable to the industry implementation of the RNF method [5]. Here we demonstrate an extension to the work presented in [5], where the refractive index profiling technique takes advantage of the data obtained across the whole DIC image and includes a full analysis along the direction of the shear of the split beam that is intrinsic to the DIC technique.

2. Differential Interference Contrast Microscopy

The Nomarski transmission DIC microscope is an interference microscope that generates high spatial resolution of a thin optical section of a transparent

specimen by exploiting optical path differences within the specimen. In a DIC microscope a two-dimensional image is formed from the interference of two mutually coherent waves that have a lateral differential displacement, $\Delta\tau$, of a few tenths of a micrometer (called the shear) that are phase shifted relative to each other. This displacement is achieved through the introduction of a Wollaston prism that splits a plane-polarized beam in two. The measured intensity in a DIC image can be written in the form given by [6,7]

$$i(x,y) = I_0 \sin^2\left(\Delta\underline{\tau}\frac{\partial}{\partial\underline{\tau}}\varphi(x,y) + \Delta\theta\right), \quad (1)$$

where I_0 is the maximum intensity transmitted by the optical system, $\varphi(x,y)$ is the phase shift introduced by the specimen, $\Delta\underline{\tau} = (\Delta\tau_x, \Delta\tau_y)$ defines the shear vector in the (x,y) plane with components $\Delta\tau_x$ across the fiber and $\Delta\tau_y$ along the fiber, and $\Delta\theta$ is a phase displacement called the bias, which is introduced by the Wollaston prism.

When imaging an optical fiber, the specimen orientation is critical and is selected based on the properties of the optical fiber being studied. In the results presented here, the fiber is positioned so that its axis is at 45° to the shear direction and orthogonal to the scan direction, preserving phase-gradient information both along and orthogonal to the axis as seen in Fig. 1. The method presented here is specific to the specimens being studied, such that we have a well-defined geometric object to investigate with no axial variation, so that no additional information could be gained (outside of the small amount of bire-

fringence) from a second DIC measurement with the shear made perpendicular to the first [8,9].

Because of the cylindrical symmetry of the fiber, it is relatively straightforward to obtain the refractive index distribution within the fiber $\Delta n(r,y)$, where r is the radial distance from the axis of the fiber, and y is the direction taken to be along the axis of the fiber. The phase shift introduced to the wave field on passing through the fiber is given by the special form of Abel's integral equation, and when inverted gives the form [10]

$$\Delta n(r,y) = -\frac{\lambda}{2\pi}\int_0^R \frac{\partial\varphi(x,y)}{\partial x}\frac{\mathrm{d}x}{\sqrt{r^2 - x^2}}, \quad (2)$$

where R is the radius of the fiber, and λ is the wavelength of the source. Thus using Eq. (2) together with the specimen's phase gradient, the refractive index distribution of the fiber can be determined. Here we perform a directional integration routine along the shear axis.

3. Materials and Methods

Two fiber specimens were considered in this work. The first was a calibrated CF2-082 multistep-index optical fiber (National Physical Laboratory [NPL]), enabling a means for testing the ability of the constructed algorithm to extract phase and refractive index information. The second specimen was a Corning SMF28 optical fiber, selected based on its wide application in optical telecommunications and optical sensing. An Olympus IX FL infinity-corrected optical system, with UplanApo 40 × /0.85 NA microscope objective, in conjunction with an argon-ion laser operating at a 488 nm wavelength, was used to acquire the DIC images. The light transmitted through the optical system was collected via a photomultiplier tube (Hamamatsu R7400U). A section of each fiber specimen was stripped of their protective jacket and immersed in index-matching oil ($n_D = 1.4580 \pm 0.0002 @ 25$ °C, Cargille Laboratories), maintained at 29.6 °C. The images were taken with a bias retardation adjusted to $\pi/2$ to achieve the best accuracy for extracting phase information [6,7,11]. To account for variations in the illumination across the field of view and to normalize the image intensity, correction images were also acquired, having bias settings of 0 and π radians.

The empirical shear between the two polarized light paths through the system can be determined by imaging a small polystyrene bead, where the lateral shift is determined by measuring the distance between the center of the bright spot and the center of the dark spot [11].

To determine the lateral shear for the system used in this work, a polystyrene bead (Polysciences, Inc. $n = 1.59$), with a diameter of $0.356\,\mu m$ was used as an approximation of a point source. The polystyrene bead was suspended in 90% ethanol and attached to a glass slide by applying a small drop, air dried, and then immersed in index-matching gel (TMT 5097,

Fig. 1. Normalized DIC image of a CF2-082 multistep-index fiber covering an area of approximately 1024 × 1024 pixels having a pixel spacing of approximately $0.23\,\mu m$.

AFC Group Pty., Ltd., $n = 1.4812$ at 488 nm). Various DIC images of the bead were then recorded with a bias set to $\pi/2$ and correction images with a bias set to 0 and π radians. To obtain an adequate representation of the DIC image of the sphere, the Nyquist theorem was satisfied [12]. The empirical shear was calculated for all the recorded images where the average shear was found to be $0.455 \pm 0.01\,\mu$m.

The algorithm to extract phase from measured DIC images was written in MATLAB version 14 (R2006a) running on a Windows XP workstation. The first optical fiber specimen considered was the calibrated CF2-082 multistep fiber where the corrected DIC image is shown in Fig. 1.

For display purposes only, a spatial bandpass filter was applied to the DIC images to reduce intensity variations in the y direction caused by fluctuating laser power. The measured DIC image in Fig. 1 shows features of artificial three-dimensional relief shading characteristic of the DIC technique. The bright and dark vertical bands in the image identify the step edges of the fiber.

To extract the phase from the measured DIC image, Eq. (1) was integrated along the direction of the shear $r_s = \Delta\tau$, where the DIC shear angle is 135° to the x axis; the extracted phase is shown in Fig. 2. The directional integration routine was applied line by line to the DIC image proceeding diagonally from the top left-hand corner to the bottom right-hand corner. Because of the uncertainty resulting from the $\pm 1\%$ rms error in the intensity values and there being an unknown integration constant for each diagonal series of pixels, streaking across the phase image in the shear direction occurs [13–

16] as seen in Fig. 2. Various methods to correct the diagonal streaking due to the random walk accumulated of uncorrelated noise along the direction of the shear and the unknown integration constant have been implemented. Kam [14] and Heise *et al.* [16] showed that by including a bidirectional exponential decay term into the line integration method, correction of the diagonal streaking was vastly improved. Additionally Arnison *et al.* [17] showed that by windowing at the same spatial frequency cutoff as that imposed by diffraction imaging, high spatial frequency artifacts introduced by the phase retrieval algorithm were minimized.

We employ a different approach to correct for nonuniformity in the background of the image and to reduce streaking artifacts caused by the numerical calculation used to retrieve the phase from the measured DIC image. The nonuniform phase, as seen in Fig. 2, is believed to be attributed to a tilt in the cover slip while acquiring the image. This artifact may later create complications in the refractive index analysis, so an averaging method was used to correct this feature. To first correct the nonuniform background in the phase image, the amplitude of the average row of the image was computed by summing down each column. This was then subtracted from each row of the image. To ensure that no specimen information is lost in the estimated background correction image, a vertical bandpass filter was then applied. The resultant background image was then used to correct the measured image as seen in Figs. 3(a)–3(c).

The filtering method used to remove specimen information from the estimated background correction image, as seen in Fig. 3(c), requires some knowledge about the specimen's geometry and spatial frequencies. Because of the symmetric geometry and size of
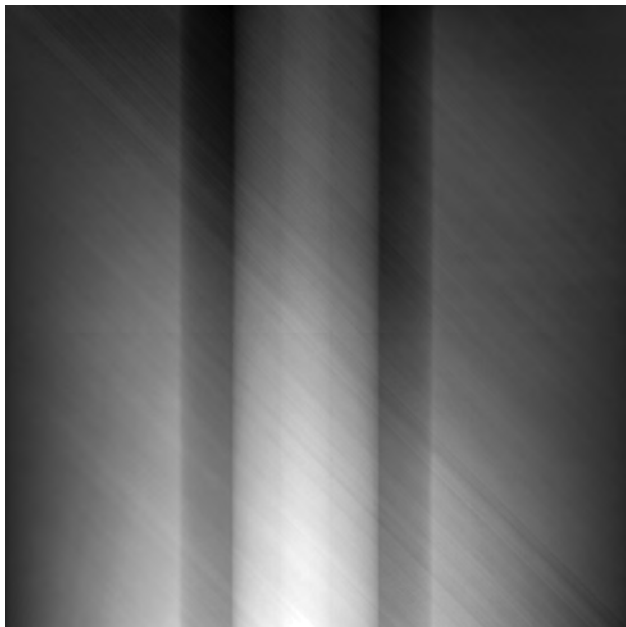

Fig. 2. Extracted phase image of a CF2-082 multistep fiber having the same dimensions as the measured image. Diagonal streaking is evident, which is due to random walk accumulation of uncorrelated noise along the direction of integration and the unknown integration constant.
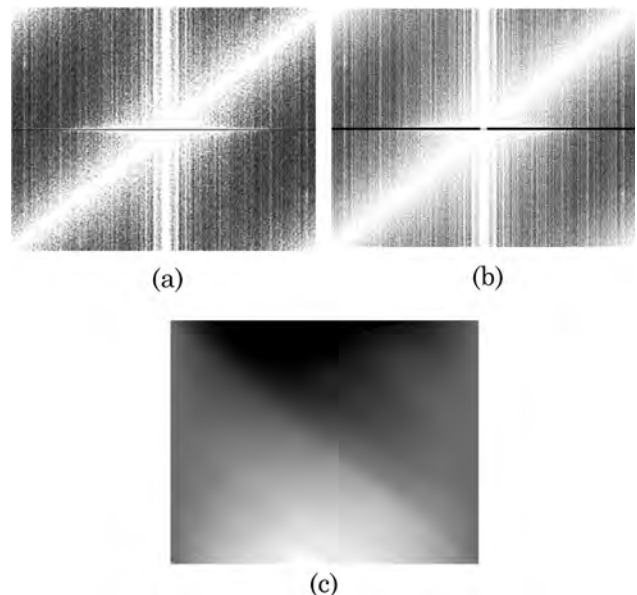

Fig. 3. (a) Two-dimensional Fourier transform of the remaining background after subtraction of the averaged row. (b) Vertical bandpass filter applied to averaged row image. (c) Resultant background image after vertical bandpass filter.

the specimen, it is fairly straightforward to eliminate specimen information in the estimated background image. However, further studies are being conducted for specimens with more complex geometries and different sizes as a means to determine the limiting factors of the background correction method used in this work.

Although this procedure corrected the image to a certain degree, horizontal nonuniformity in the background remained. To further correct this nonuniformity, a horizontal line profile from the corrected image was selected, and regions of the background (i.e., regions of the image not containing specimen information) were selected. A cubic polynomial was then fitted to the horizontal line profile extracted from the image [18]. The fitted polynomial was then subtracted from every row of the image, resulting in the data of Fig. 4(a).

To verify the accuracy of our routines, the calibrated multistep fiber was simulated using the refractive index differences provided in the fiber's calibration certificate, where the diameters of each region of the fiber were calculated from the measured image as shown in Fig. 4(b). The representation of refractive index of the surrounding medium in the simulated image was set at a refractive index difference of 5×10^{-5} with respect to the cladding.

The simulation used the same imaging parameters as the measured image (with a wavelength of 488 nm), a lateral shear of $0.455 \pm 0.01\,\mu$m, and a pixel spacing of $0.23\,\mu$m. The simulated multistep fiber was considered to have the fiber structure schematically represented in Fig. 5. The induced phase delay travelling through the uniform fiber can be expressed by
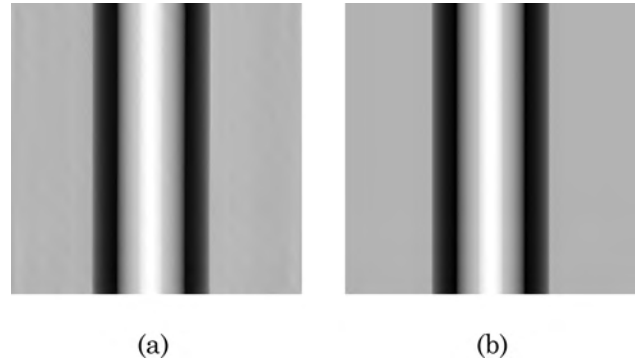

Fig. 4. (a) Extracted phase image of the CF2-082 multistep fiber from the measured DIC image after a third-degree polynomial fit was applied to remove horizontal nonuniformity of the background illumination in the phase image. (b) Simulated phase image of the CF2-082 multistep fiber modeled to replicate the same imaging conditions as the measured DIC image covering an area of 1024 × 1024 pixels having a pixel spacing of approximately $0.23\,\mu$m.

profile through both images was taken and is shown in Fig. 6.

As can be seen from Fig. 6, the measured and simulated phase images show good agreement; however, a small discrepancy appears at the interface between the fiber's cladding and the surrounding medium. This was due to a small mismatch in the set refractive index value of the surrounding medium in the simulated image.

The refractive index profile was then determined using the extracted phase and the implementation of Eq. (2) and is shown in Fig. 7, where Fig. 7(a) shows the surface plot of the change in refractive index of the CF2-082 multistep fiber from the cladding

$$
\left\{
\begin{array}{ll}
2k_0(n_1\sqrt{R_1^2 - x^2}) + k_0 n_0(d - 2\sqrt{R_4^2 - x^2}) & \text{for} \quad R_4 \leq |x| \leq R_1 \\[2ex]
2k_0 n_4(\sqrt{R_4^2 - x^2}) + 2k_0 n_3(\sqrt{R_3^2 - x^2} - \sqrt{R_4^2 - x^2})) & \\
+2k_0 n_2(\sqrt{R_2^2 - x^2} - \sqrt{R_3^2 - x^2}) + 2k_0 n_1(\sqrt{R_1^2 - x^2} & \\
-\sqrt{R_2^2 - x^2}) + k_0 n_0(d - 2\sqrt{R_1^2 - x^2}) & \text{for} \quad |x| \leq R_1
\end{array}
\right\}, \quad (3)
$$

where R_1 through R_4 are the radii of regions I to IV, n_1 to n_4 is the refractive index of regions I to IV, and n_0 is the refractive index of the surrounding medium as seen in Fig. 5.

The phase amplitude was determined for both the measured image and the simulated image to ensure that no artifacts were introduced during the preprocessing stages of the extracted phase from the measured DIC image. The results indicate that the image processing procedures did not alter the phase amplitude. To compare the extracted phase from the measured DIC image to the simulated image, a line

index as a function of position. The transverse profile averaged over Fig. 7(a) is shown in Fig. 7(b) and compared with the recovered refractive index profile of the simulated image of the multistep fiber, where the error bars represent the standard deviation of the upper and lower bounds of the refractive index profile determined by the error in the calculated shear.

A comparison of the refractive index profile from the simulated and measured image [Fig. 7(b)] indicates that the major discrepancy lies with the flatness of the different regions of the fiber. The nonuniformity of region II was also observed using
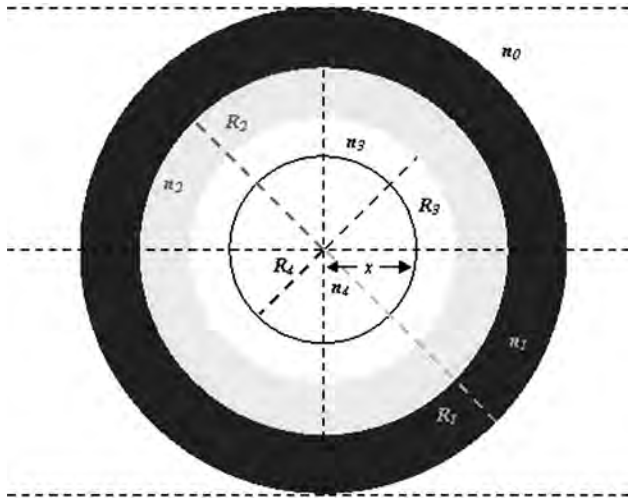
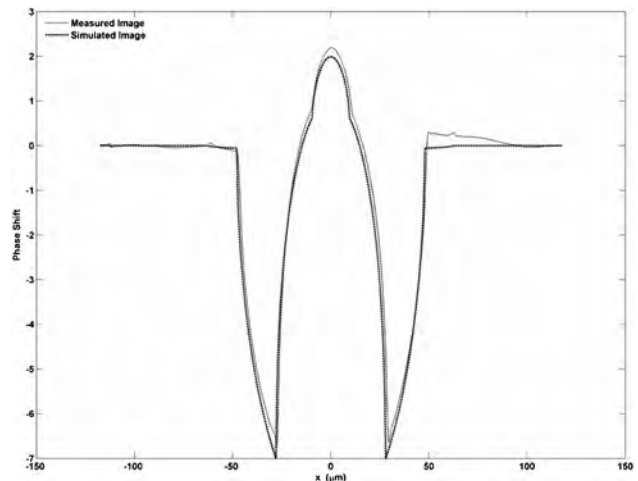Fig. 5. Schematic representation of the multistep fiber structure.

Fig. 6. Line profile through the phase image of a multistep fiber obtained from simulated and experimentally obtained data, where the solid curve represents the extracted phase profile from the measured DIC image, and the dotted curve represents the phase profile through the simulated phase image.

qualitative phase microscopy and atomic force microscopy [19], which suggests that this effect is not an imaging artifact nor resultant of the limiting ability of the algorithm, but rather intrinsic to the fiber itself. Additionally Gibb's phenomenon [20,21] can be observed in the simulated image due to the abrupt step changes in the fiber refractive indices, which is unavoidable for a true step-index fiber. An artifact at zero radius is observed in the profile extracted from the simulated image. This is inherent to the radial calculation method of Eq. (2). The refractive index difference between each region was calculated from each measured profile and was determined by finding the average value within each region. The error associated with these values was determined by the standard deviation of the upper and lower bounds of the refractive index profile determined by the error in the calculated shear and is shown in Table 1.

Comparison of the refractive index differences of each region determined from the measured DIC image are in good agreement with the manufacturer's results as shown in Table 1. Systematic differences between the calibrated results (measured using axial interferometry and the RNF technique) and the results of the technique presented here may be primarily attributed to the different operating wavelength employed by the measurement devices. The manufacturer's results were taken at a wavelength of 633 nm in comparison to the results here conducted with an argon-ion laser operating at 488 nm. Another possible source of error could be deviations from the concentricity of the fiber. The concentricity of the fiber was measured and found to vary by 0.01%, suggesting this would not contribute significantly to the deviations of the refractive index differences from the manufacturer's specifications.

Although the results presented here show excellent agreement with the manufacture's results, the
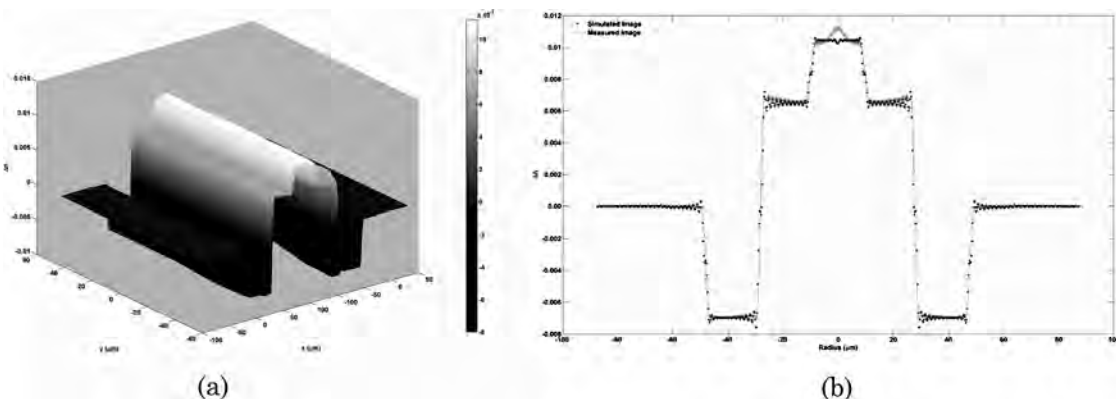

Fig. 7. Refractive index profile obtained from the phase image shown in Fig. 4(a). (a) Surface plot of the change in refractive index through the various regions of the fiber as a function of position, where the color bar displays the change in refractive index. (b) Line profile through the simulated and extracted refractive index distribution of the multistep fiber, where I–IV specify the varying regions of the fiber. The point plot represents a line profile through the refractive index distribution from the simulated image, and the solid curve represents a line profile through the refractive index distribution from the measured image.

Table 1. Comparison between the Refractive Index Differences for the Radial Integration Method Applied to a Measured Differential Interference Contrast Image with the Specifications of the Calibrated Multistep Fiber

	λ (nm)	Refractive Index Difference (Δn)			
		Levels I–II	Levels II–III	Levels II–IV	Levels III–IV
DIC	488	-0.0068 ± 0.0015	0.01326 ± 0.0003	0.01685 ± 0.0004	0.00358 ± 0.00008
RNF and Axial Interferometry	633	-0.0074 ± 0.0001	0.01395 ± 0.00015	0.01785 ± 0.00015	0.00395 ± 0.00005

intrinsic birefringence of the specimens used in this work, similar to those previously measured, are considered to be low, of the order of 10^{-5} [8,9,22–25]. Therefore only a very small variation in the refractive index profile in the transverse and longitudinal plane will be present. This approximation, however, limits the work presented here, where its application may only be applicable to specimens with low birefringence.

The next specimen investigated was a Corning SMF28 optical fiber. To acquire the DIC image of this specimen, the same optical system and imaging conditions were used. The fiber was immersed in the same index-matching oil, for which for a match to the fiber cladding index was obtained at a temperature of 29.3 °C. Again the image was taken with a bias set to $\pi/2$ with correction images taken with a bias set to 0 and π radians; the resultant image is shown in Fig. 8.

The phase was extracted from the measured DIC image using the directional integration algorithm and processing procedures as described for the NPL fiber and is shown in Fig. 9. The amplitude of the refractive index profile of the fiber was measured independently using a York S14 fiber RI pro-

filer at the Laboratoire de Physique de la Matière Condensèe, Nice, France.

The refractive index profile of the specimen was evaluated from the extracted phase of the measured DIC image and the difference between the maximum core refractive index and that of the cladding (found to be 0.0053 ± 0.00012) and was compared with a profile obtained from a commercial profiler as shown in Fig. 10(b). As seen from Fig. 10(a), this method can determine the axial variations in the refractive index, and in Fig. 10(b) the transverse index averaged over Fig. 10(a) is shown. This method can be used to visualize axial variation in the extracted phase images, where the image is computed by a series of many diagonal integrated lines of the DIC image. One may then compare successive columns and rows, by which knowledge is gained of the direction of the refractive index variation. It should be noted that axial variations in the direction of the shear are not recorded. Thus the refractive index profile may be determined for specimens that exhibit axial variations such as FBGs . However, this is only true if the variations along the specimen's axis are symmetrical; in the case of FBGs, previous work has
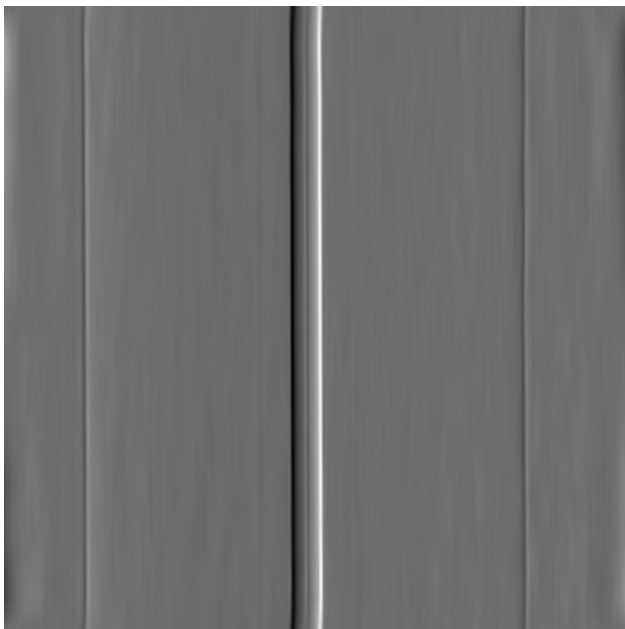

Fig. 8. Normalized DIC image of the Corning SMF28 optical fiber covering an area of approximately 1024×1024 pixels having a pixel spacing of approximately $0.173\,\mu m$.
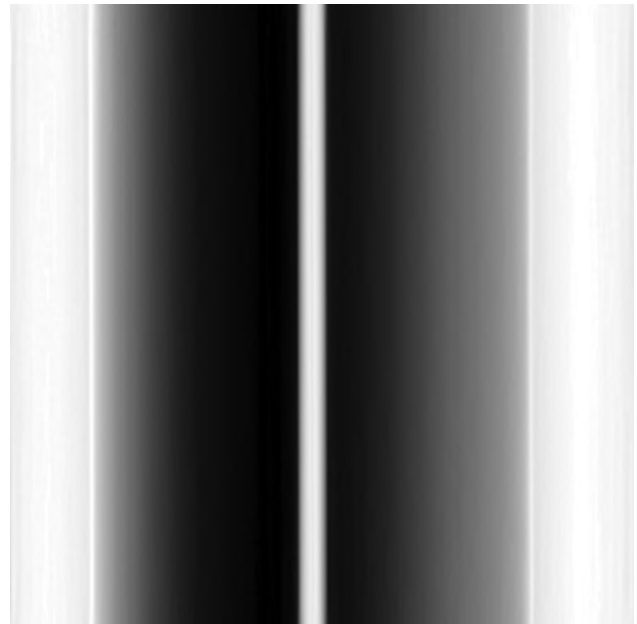

Fig. 9. Extracted phase image of the SMF28 optical fiber from the measured DIC image, where a third-degree polynomial fit is applied to the outer boundaries of the fiber to correct uneven illumination in the phase image
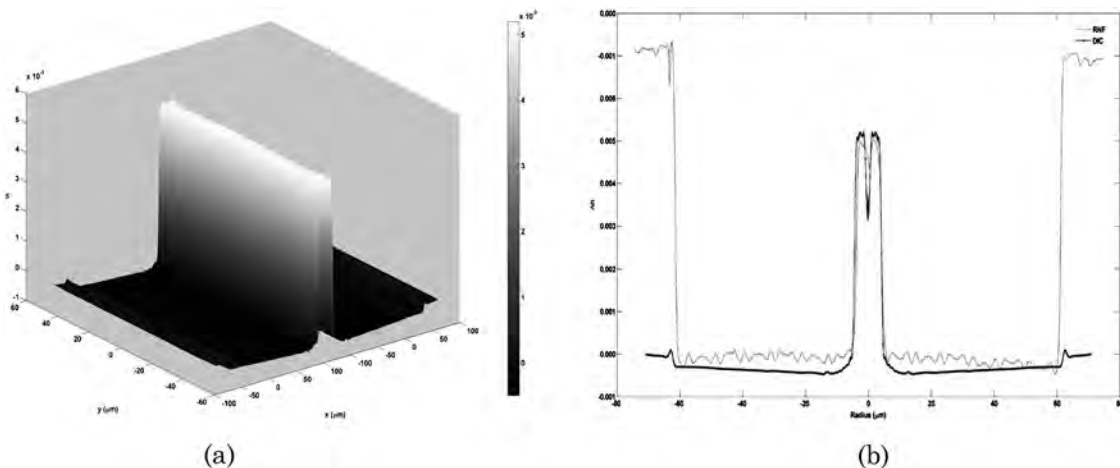
Fig. 10. Refractive index profile obtained from the phase image shown in Fig. 10. (a) Surface plot of the change in refractive index from the cladding as a function of position, where the color bar displays the varying colors used to highlight the change in refractive index. (b) Line profile through the extracted refractive index distribution of the SMF28 optical fiber. The dotted curve represents a line profile through the refractive index distribution from RNF method, and the solid curve represents a line profile through the refractive index distribution calculated from the measured image.

revealed that the axial variations induced during fabrication of these optical devices possess both longitudinal and lateral structure [26,27]. Although the method presented here can extract the phase of the measured DIC image of such a structure, alternative methods to the inverse Abel transform need to be employed to determine the refractive index.

To determine the apparent variation in refractive index in a uniform region of the fiber and to give a estimate of the sensitivity of our method, a rectangular region in the cladding region of Fig. 10(a) was taken, and the standard deviation of the refractive index variation was determined and found to be 4.82×10^{-5}. This result suggests that the methods used in this work to extract the phase and refractive index information of our specimens has minimal susceptibility to noise variation. Although very small, the error bars shown in Fig. 10(b) represent the standard deviation of the upper and lower bounds of the refractive index profile determined by the error in the calculated shear.

As can be seen from Fig. 10(b), the refractive index profile extracted from the measured DIC image and the profile obtained from the commercial profiler are in excellent agreement. Furthermore the results are in excellent agreement with the fiber's specifications, where a refractive index difference of 0.36% is expected. It can be seen from Fig. 10(b) that the refractive index of the cladding region obtained using the RNF technique appears to fluctuate more than the results evaluated using the routine presented here, which may suggest either that the RNF technique has a higher sensitivity to small phase shifts or is more subject to noise variation in the analysis process. Furthermore our results in the cladding region exhibit a slight slope in the refractive index variation; however, this is believed to be an artifact resulting from a tilt in the specimen, as can be detected in the measured DIC image of Fig. 8.

4. Conclusion

A method to determine the phase and refractive index profile of optical fiber specimens using a standard commercial DIC microscope without the insertion of any further optics has been presented. It builds on the work presented in [5]; however, this work takes advantage of data across the whole DIC image and includes a full analysis along the direction of the shear of the split beam. Results extracted from the measured DIC image of a calibrated multistep fiber are in agreement with the manufacturer's specifications, evaluated using the RNF and axial interferometry technique. Furthermore results of the refractive index profile of a Corning SMF28 singlemode fiber show excellent agreement with independent results obtained using the RNF technique.

The method presented here for the retrieval of phase and refractive index data of optical fibers is limited to specimens with low birefringence. Further work is being conducted to analyze the limitations of the background subtraction method presented for the correction of nonuniform background and streaking artifacts introduced from numerical calculations. Additionally the applicability of this method with optical fibers with a varying refractive index modulation in the core, such as FBGs, will be analyzed. These further results will give more complete insight to the limiting factors of the proposed method.

References

1. K. I. White, "Practical application of the refracted near-field technique for the measurement of optical fibre refractive index profiles," Opt. Quantum Electron. **11**, 185–196 (1979).

2. K. W. Raine, J. G. N. Baines, and D. E. Putland, "Refractive index profiling-state of the art," J. Lightwave Technol. **7**, 1162–1169 (1989).

3. A. Roberts, E. Ampem-Lassen, A. Barty, K. A. Nugent, G. W. Baxter, N. M. Dragomir, and S. T. Huntington, "Refractive-index profiling of optical fibers with axial symmetry by use of quantitative phase microscopy," Opt. Lett. **27**, 2061–2063 (2002).

4. E. Ampem-Lassen, S. T. Huntington, N. M. Dragomir, K. A. Nugent, and A. Roberts, "Refractive index profiling of axially symmetric optical fibers: a new technique," Opt. Express **13**, 3277–3282 (2005).

5. N. M. Dragomir, E. Ampem-Lassen, S. T. Huntington, G. W. Baxter, A. Roberts, and P. M. Farrell, "Refractive index profiling of optical fibers using differential interference contrast microscopy," IEEE Photon. Technol. Lett. **17**, 2149–2151 (2005).

6. M. Pluta, *Advanced Light Microscopy* (Elsevier, 1988).

7. C. Preza, "Phase estimation using rotational diversity for differential interference contrast microscopy," D.Sc. thesis (Washington University, Sever Institute of Technology, St. Louis, Mo., 1998).

8. W. Urbanczyk and K. Pietraszkiewicz, "Measurements of stress anisotropy in fiber preform: modification of the dynamic spatial filtering technique," Appl. Opt. **27**, 4117–4122 (1988).

9. W. Urbanczyk, K. Pietraszkiewicz, and W. A. Wozniak, "Novel bifunctional systems for measuring the refractive index profile and residual stress birefringence in optical fibers and preforms," Opt. Eng. **31**, 491–499 (1992).

10. M. Kalal and K. A. Nugent, "Abel inversion using fast Fourier transforms," Appl. Opt. **27**, 1956–1959 (1988).

11. E. B. Van Munster, L. J. Van Vliet, and J. A. Aten, "Reconstruction of optical pathlength distributions from images obtained by a wide-field differential interference contrast microscope," J. Microsc. **188**, 149–157 (1997).

12. M. Born and E. Wolf, *Principles of Optics: Electromagnetic Theory of Propagation, Interference and Diffraction of Light*, 3rd ed. (Pergamon, 1965), pp. xxviii and 808.

13. C. J. Cogswell, N. I. Smith, K. G. Larkin, and P. Hariharan, "Quantitative DIC microscopy using a geometric phase shifter," Proc. SPIE **2984**, 72–81 (1997).

14. Z. Kam, "Microscopic differential interference contrast image processing by line integration (LID) and deconvolution," Bioimaging **6**, 166–176 (1998).

15. W. Shimada, T. Sato, and T. Yatagai, "Optical surface microtopography using phase-shifting Nomarski microscope," Proc. SPIE **1332**, 525–529 (1991).

16. B. Heise, A. Sonnleitner, and P. E. Klement, "DIC image reconstruction on large cell scans," Microsc. Res. Tech. **66**, 312–320 (2005).

17. M. R. Arnison, K. G. Larkin, C. J. R. Sheppard, N. I. Smith, and C. J. Cogswell, "Linear phase imaging using differential interference contrast microscopy," J. Microsc. **214**, 7–12 (2004).

18. B. P. Kouskousis, D. J. Kitcher, S. F. Collins, A. Roberts, and G. W. Baxter, "Refractive index profile of a multi-step fibre using differential interference contrast microscopy," in COIN-ACOFT 2007, Melbourne, Australia, 2007.

19. E. Ampem-Lassen, "Studies in photonic device imaging and characterisation," Ph.D. dissertation (University of Melbourne, School of Physics, 2004).

20. J. G. Wanguemert-Perez, R. Godoy-Rubio, A. Ortega-Monux, and I. Molina-Fernandez, "Removal of the Gibbs phenomenon and its application to fast-Fourier-transform-based mode solvers," J. Opt. Soc. Am. A **24**, 3772–3780 (2007).

21. D. Gottlieb and C. W. Shu, "On the Gibbs phenomenon and its resolution," SIAM Rev. **39**, 644–668 (1997).

22. K. Dossou, S. LaRochelle, and M. Fontaine, "Numerical analysis of the contribution of the transverse asymmetry in the photo-induced index change profile to the birefringence of optical fiber," J. Lightwave Technol. **20**, 1463–1470 (2002).

23. O. H. Waagaard, "Polarization-resolved spatial characterization of birefringent fiber Bragg gratings," Opt. Express **14**, 4221–4236(2006).

24. P. Lu, D. Grobnic, and S. J. Mihailov, "Characterization of the birefringence in fiber Bragg gratings fabricated with an ultrafast-infrared laser," J. Lightwave Technol. **25**, 779–786 (2007).

25. J. Canning, H. J. Deyerl, H. R. Sorensen, and M. Kristensen, "Ultraviolet-induced birefringence in hydrogen-loaded optical fiber," J. Appl. Phys. **97**, 53104 (2005).

26. N. M. Dragomir, C. Rollinson, S. A. Wade, A. J. Stevenson, S. F. Collins, G. W. Baxter, P. M. Farrell, and A. Roberts, "Nondestructive imaging of a type I optical fiber Bragg grating," Opt. Lett. **28**, 789–791 (2003).

27. B. P. Kouskousis, C. M. Rollinson, D. J. Kitcher, S. F. Collins, G. W. Baxter, S. A. Wade, N. M. Dragomir, and A. Roberts, "Quantitative investigation of the refractive-index modulation within the core of a fiber Bragg grating," Opt. Express **14**, 10332–10338 (2006).